Three-way comparison between OMI and PARASOL cloud pressure products

M. Sneep,[1] J. F. de Haan,[1] P. Stammes,[1] P. Wang,[1] C. Vanbauce,[2] J. Joiner,[3] A. P. Vasilkov,[4] and P. F. Levelt[1]

Received 23 March 2007; revised 19 September 2007; accepted 30 October 2007; published 14 May 2008.

[1] The cloud pressures determined by three different algorithms, operating on reflectances measured by two spaceborne instruments in the "A" train, are compared with each other. The retrieval algorithms are based on absorption in the oxygen A-band near 765 nm, absorption by a collision induced absorption in oxygen near 477 nm, and the filling in of Fraunhofer lines by rotational Raman scattering near 350 nm. A Lambertian reflector as cloud model is assumed in the retrievals. The first algorithm operates on data collected by the POLDER instrument on board PARASOL, while the latter two operate on data from the OMI instrument on board EOS-Aura. The satellites sample the same air mass within about 15 min. We compare the retrieval algorithms using synthetic spectra to give the comparison realistic baseline expectations. It appears that these cloud pressures are not the pressure of the cloud top, but of a level inside the cloud. This is corroborated by comparisons with MODIS and CloudSat data: while the top of the cloud is seen by MODIS using emitted IR radiation, both OMI and PARASOL algorithms retrieve a pressure near the midlevel of the cloud. The three cloud pressure products are compared using 1 month of data. The cloud pressures are found to show a similar behavior, with correlation coefficients larger than 0.85 between the data sets for high effective cloud fractions. The average differences in the cloud pressure are small, between 2 and 45 hPa, for the whole data set, with an RMS difference of 65 to 93 hPa. This falls within the science requirement for the OMI cloud pressure to have an accuracy of 100 hPa. For small to medium effective cloud fractions, the cloud pressure distribution found by PARASOL is very similar to that found by OMI using the O_2–O_2 absorption. Somewhat larger differences are found for very high effective cloud fractions.

Citation: Sneep, M., J. F. de Haan, P. Stammes, P. Wang, C. Vanbauce, J. Joiner, A. P. Vasilkov, and P. F. Levelt (2008), Three-way comparison between OMI and PARASOL cloud pressure products, *J. Geophys. Res.*, *113*, D15S23, doi:10.1029/2007JD008694.

1. Introduction

[2] Clouds have a large influence on the transfer of radiation in the atmosphere, making proper cloud detection and correction important for trace gas retrievals in passive remote sensing. Passive remote sensing instruments designed to detect clouds can provide a large set cloud properties: particle phase, particle radius, cloud liquid- or ice-water content, cloud optical thickness, and cloud (top) pressure or cloud (top) temperature. These properties are usually observed using a combination of wavelength bands in the visible and thermal infrared part of the spectrum. For the cloud correction of trace gas retrievals from UV/VIS reflectance spectra a much simpler cloud model is commonly used. For trace gas correction clouds are represented by a Lambertian surface described by an effective cloud fraction and a cloud pressure [*Koelemeijer and Stammes*, 1999; *Ahmad et al.*, 2004; *Liu et al.*, 2004]. These parameters are found from a fit of the observed top-of-atmosphere reflectance, and the strength of a height-sensitive spectral feature. In the present article we compare cloud pressure data from two satellite instruments flying in the "A" train, using 1 month of data with global coverage.

[3] This comparison includes three cloud products: cloud pressure derived from the O_2 A-band absorption at 765 nm, cloud pressure derived from O_2–O_2 absorption at 477 nm and cloud pressure derived from the filling in of Fraunhofer lines by rotational Raman scattering at 350 nm. The first is observed by the POLDER (Polarization and Directionality of the Earth's Reflectances) instrument on PARASOL (Polarization and Anisotropy of Reflectances for Atmospheric Sciences coupled with Observations from a Lidar), the latter two are observed from OMI (Ozone Monitoring Instrument) on EOS Aura. PARASOL is specifically designed to study cloud and aerosol properties from space, while OMI is designed to measure reflectance spectra with a

[1]Climate Research and Seismology Department, Royal Netherlands Meteorological Institute, De Bilt, Netherlands.
[2]Laboratoire d'Optique Atmosphérique, Université des Sciences et Technologies de Lille, CNRS, Lille, France.
[3]NASA Goddard Space Flight Center, Greenbelt, Maryland, USA.
[4]Science Systems and Applications, Inc., Lanham, Maryland, USA.

Copyright 2008 by the American Geophysical Union.
0148-0227/08/2007JD008694

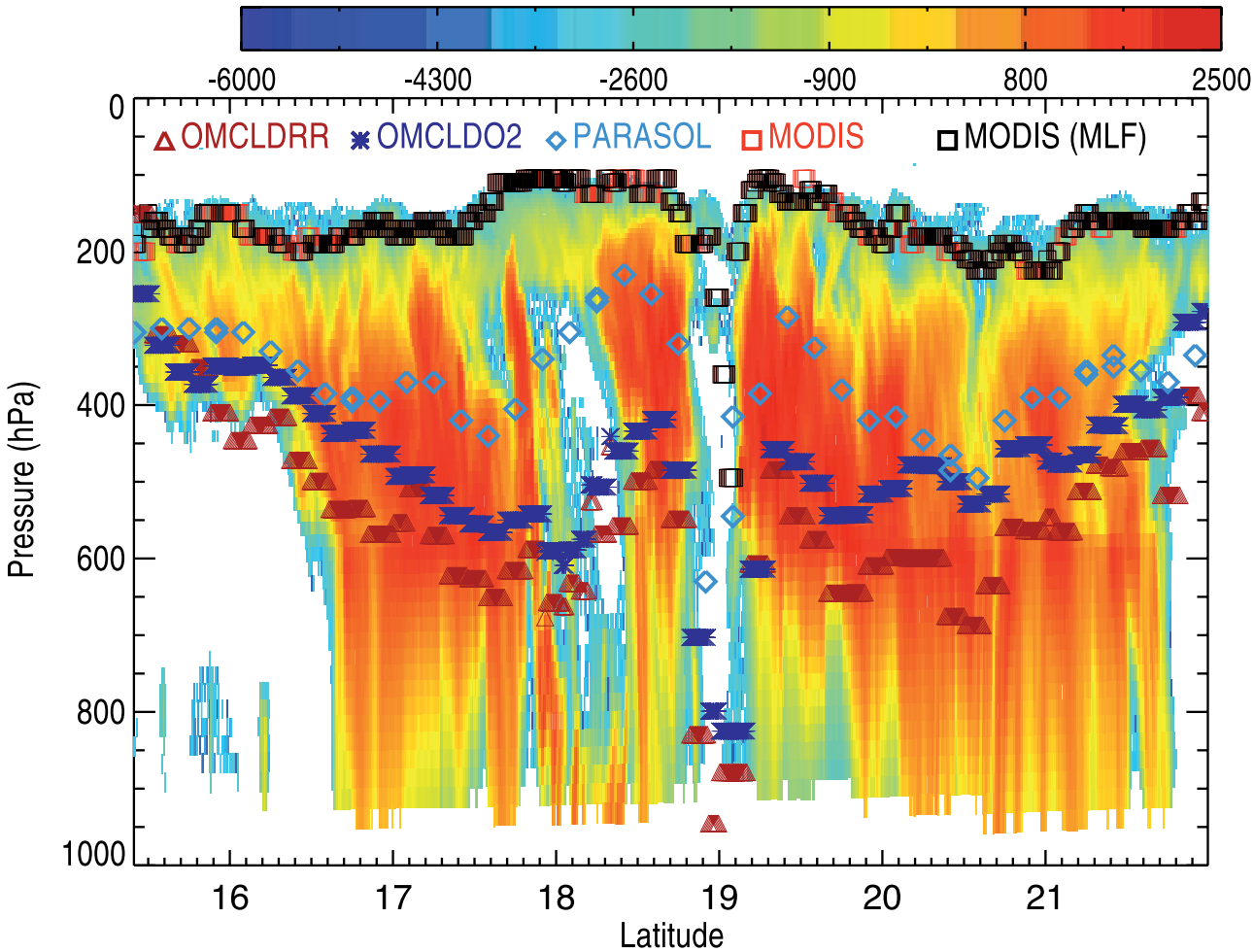

Figure 1. CloudSat profiles through hurricane Ileana, with the cloud pressures from OMCLDO2, OMCLDRR, PARASOL, and MODIS (with and without Multi-Layer-Flag, MLF) plotted on top of them. The CloudSat radar reflectivity is indicated by the color bar, in arbitrary units.

high spectral resolution to perform atmospheric composition measurements.

[4] This study is part of the larger validation effort of OMI and EOS Aura. For trace gas retrievals, the cloud parameters are one of the most important error sources, and as such the cloud products deserve special attention. A study on the influence of the cloud parameters on ozone retrieval is presented by *Stammes et al.* [2008].

[5] The products involved in the comparison retrieve the cloud pressure from a photon path length determined from top of atmosphere reflectance spectra, and therefore no truly independent validation takes place in this study. This comparison provides a means to assess the quality of OMI cloud pressure retrievals through an internal consistency check. This type of comparison is particularly important, because comparisons with thermal infrared retrievals are hard to interpret because of the different scattering properties of the two types of radiation; thermal infrared is strongly absorbed in liquid water and ice, while UV/VIS radiation penetrates more deeply inside the cloud. *Koelemeijer and Stammes* [1999], *Wang et al.* [2006a], *Vasilkov et al.* [2008], and *Stammes et al.* [2008] show that the cloud pressure which minimizes the errors on ozone retrieval is the cloud pressure derived from UV/VIS, which is well below the cloud top.

[6] Even though the photon path lengths are similar, the wavelengths at which the cloud pressures were determined are quite different. At the PARASOL wavelength, the surface albedo is a difficult issue, especially over land. This is much less the case for the OMI wavelengths. If the cloud pressure comparisons do not show a significantly different result over land compared to those over sea then this implies that the surface correction by the PARASOL algorithm is of good quality.

[7] The CloudSat measurements shown in the last section can be used as an independent data source for validation of the cloud pressure products from the A train. At this stage not nearly enough CloudSat data has been compared to OMI and PARASOL to gather enough statistics for meaningful results; Figure 1 serves only as an illustration.

[8] The structure of this paper is as follows. The next section briefly describes the two instruments, followed by a section on the cloud retrieval algorithms, including results obtained using synthetic spectra. Next is a short section on the collocation of measurements from OMI to measurements from PARASOL, followed by a description of the actual

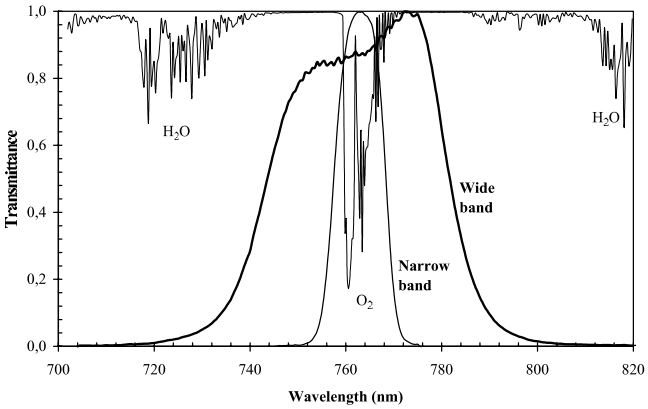

Figure 2. PARASOL filter transmissions in the narrow and wide bands centered at 763 nm and 765 nm, respectively, together with atmospheric transmission in the oxygen A-band region.

comparison results. We end with a discussion of the similarities and differences we observe, and a brief discussion of future improvements.

2. Description of the Instruments

[9] Both EOS Aura and PARASOL are part of the so called "A" train, a series of satellites carrying Earth observation instruments. Near the front of the train is the PARASOL satellite with its POLDER instrument. For brevity we will refer to this instrument as PARASOL, since POLDER is the only instrument on this satellite, and this avoids confusion with earlier POLDER instruments. The last satellite in the A train is EOS Aura, which carries four instruments, including OMI. This instrument is briefly described in section 2.2. Both instruments sample the same part of the atmosphere within approximately 15 min. PARASOL crosses the equator at about 1330 local solar time; EOS Aura crosses the equator at about 1340 local solar time.

2.1. Description of PARASOL

[10] The PARASOL scientific objectives are to characterize the radiative and microphysical properties of clouds and aerosols. PARASOL is carrying a wide-field imaging radiometer/polarimeter called POLDER which is extensively described by *Deschamps et al.* [1994]. Algorithms dedicated to Earth radiation budget, water vapor, and clouds were developed, taking into account the PARASOL capabilities [*Buriez et al.*, 1997]. Daily products and monthly syntheses are produced at 18×18 km^2 resolution (after cloud detection performed at full resolution, 6×6 km^2, and for every direction). The data archive starts from 4 March 2005, and PARASOL is still operational at present time.

2.2. Description of OMI

[11] The Ozone Monitoring Instrument (OMI) is a contribution of the Netherlands' Agency for Aerospace Programs (NIVR) in collaboration with the Finnish Meteorological Institute (FMI) to NASA's EOS Aura mission. OMI will continue the TOMS satellite data record for total ozone and other atmospheric parameters related to ozone chemistry, air quality and climate. The OMI instrument observes solar backscattered radiation in the visible and ultraviolet, covering the wavelength range 270 nm to 500 nm, with a spectral resolution of 0.42–0.63 nm. The swath is wide enough to allow for global coverage in 1 d (14 orbits), with a spatial resolution of 13×24 km^2 for nadir observations. The spectral range and resolution of OMI allows for the retrieval of column amounts of atmospheric trace gases, like O_3, NO_2, SO_2, BrO, HCHO. Estimates of cloud parameters are needed for the trace gas retrievals in cloudy pixels. A detailed description of the OMI instrument and its science objectives is given by *Levelt et al.* [2006a, 2006b].

3. Short Overview of the Cloud Pressure Retrieval Algorithms

[12] Two of the retrieval algorithms use absorption of radiation by oxygen, while the third uses the amount of filling in of Fraunhofer lines due to rotational Raman scattering to determine the cloud pressure. They all use reflected sunlight, rather than thermal infrared emissions from clouds, as is done in most meteorological satellite retrieval techniques for cloud top temperature and cloud top pressure.

[13] Both OMI cloud products use basically the same cloud model, which is the same as that used in FRESCO [*Koelemeijer et al.*, 2001]. The cloud is represented by a Lambertian surface with albedo 0.8; that is, no light is transmitted through the cloud. The scene is partially covered by the model cloud with an effective cloud fraction c_{eff}, so that the top-of-atmosphere reflectance agrees with the observed reflectance. The albedo of the model cloud is so high that most scenes have an effective cloud fraction less than one; the missing transmission of this model cloud is compensated by the large cloud-free part of the pixel. The cloud pressure p_c is adjusted to that the depth of a spectroscopic feature matches the observed strength of that feature.

[14] The cloud model used in PARASOL is somewhat different. Over sea, where the surface is very dark at 765 nm, the cloud optical thickness determined from other channels on board PARASOL is used as a threshold value in determining the cloud pressure p_{c}. This cloud pressure is here equal to an apparent pressure which means that over sea the cloud model is a Lambertian surface with albedo 1, which is quite similar to the model used in OMI. Over land, where the surface can be very bright at 765 nm, especially over vegetation, the cloud optical thickness is used both for selection and correction of p_{app}. The cloud model used in this correction is very different from the OMI cloud model, namely a scattering and transmitting cloud.

3.1. PARASOL Cloud Pressure Retrieval Using the Oxygen A-Band at 765 nm

[15] Two different methods were developed to retrieve cloud pressure from PARASOL data [*Buriez et al.*, 1997]. The first one (cloud Rayleigh pressure) is based on the analysis of polarized reflected light at 490 nm, and is not discussed further in the present article. The second one (cloud oxygen pressure) uses the ratio of the two PARASOL

radiances measured in the oxygen A-band near 765 nm. Cloud oxygen pressure p_{O_2} is determined from differential absorption between the radiances measured in the channels centered at 763 nm (narrow band) and 765 nm (wide band) respectively (see Figure 2). The R_{763} and R_{765} radiances are first corrected for gaseous absorption of ozone and water vapor, then the measured oxygen transmittance T_{O_2} is obtained from the ratio of R_{763} and R_{765}. All the gaseous transmissions are derived from simulations using a line-by-line model [*Scott*, 1974]. The spectroscopic database used for the absorption cross sections is HITRAN 2004 [*Rothman et al.*, 2005]. In the first step, the influence of the surface albedo is neglected, and the cloud model used in this step is a Lambertian reflector with albedo 1. An apparent pressure p_{app} is inferred by assuming that the atmosphere behaves as a pure absorbing medium overlying such a cloud located at pressure p_{app}. In practice, p_{app} is calculated from a polynomial function of T_{O_2} and the geometric air mass factor $M = 1/\cos\theta + 1/\cos\theta_0$, with θ and θ_0 the viewing and solar zenith angles. The coefficients of the polynomials are fitted from line-by-line calculations.

[16] Because of enhanced oxygen absorption due to the effects of surface reflection and multiple scattering inside the cloud, the apparent pressure p_{app} is almost always higher than the cloud top pressure. For example, even for optically thick clouds, large differences (typically 200 hPa) were observed between POLDER-1 apparent pressures and cloud top pressures derived from the brightness temperatures measured in the 11 μm channel of METEOSAT [*Vanbauce et al.*, 1998]. The apparent pressure can even be higher than the cloud base pressure when a great amount of photons reaches the surface before being reflected back to space, as in the case of a thin cloud layer above a bright surface. Cloud oxygen pressure p_{O_2} is determined from the apparent pressure by removing the surface contribution, see *Vanbauce et al.* [2003] for details. This correction is only realized for pixels over land surface, because the ocean reflectance is low at 765 nm and therefore the surface influence is negligible.

[17] In the operational algorithm, p_{O_2} is calculated only for cloudy pixels with optical thickness larger than 3.5. The cloud pressures retrieved from different viewing angles are averaged, and then the results for the cloudy 6×6 km^2 subpixels are combined into the final cloud pressure at 18×18 km^2 pixels. The cloud optical thickness used for scene selection is derived from PARASOL measurements at 670 nm over land and 865 nm over ocean from radiative transfer modeling based on the plane-parallel hypothesis [*Buriez et al.*, 1997, 2005].

[18] From comparisons of POLDER-1 cloud oxygen pressure and ARM/MMCR cloud top and bottom pressures [*Clothiaux et al.*, 2000], p_{O_2} appears to indicate the cloud middle pressure rather than the cloud top pressure [*Vanbauce et al.*, 2003].

3.2. OMI Cloud Pressure Retrieval Using the Collision Induced Absorption in Oxygen at 477 nm

[19] Only a brief overview of the OMI O_2–O_2 cloud model and cloud retrieval algorithm (officially named "OMCLDO2") will be given here, since they are described in considerable detail by *Acarreta et al.* [2004]. The A, B, and γ absorption bands in molecular oxygen all fall outside the wavelength range of OMI. This means that the FRESCO method for cloud pressure detection, which is used for GOME and SCIAMACHY is not readily available for OMI. However, oxygen has several collision induced absorption (CIA) features within the OMI wavelength range, and they may be used instead. In these CIA features two oxygen molecules jointly absorb a single photon, and both fly away from the collision in an (electronically) excited state. The strongest of these CIA features within the OMI wavelength range is found at 477 nm, see for instance *Greenblatt et al.* [1990].

[20] A DOAS (Differential Optical Absorption Spectroscopy [*Platt*, 1994]) fit of the OMI reflectance spectrum between 460 and 490 nm is used to determine the slant column amount of O_2–O_2. This value, combined with the viewing and solar geometry and surface conditions, is used to find the cloud pressure with the aid of a lookup table. The lookup table was produced with the DAK (Doubling Adding KNMI [*de Haan et al.*, 1987; *Stammes*, 2001]) radiative transfer model, using a Lambertian surface with albedo 0.8 as the cloud model. The continuum reflectance of the scene, combined with the surface albedo from a climatology derived from GOME measurements, is used to determine the effective cloud fraction c_{eff}.

[21] Since the first description of the O_2–O_2 cloud retrieval algorithm [*Acarreta et al.*, 2004], some aspects of the retrieval algorithm were changed. Rather than the logarithm of the reflectance as in *Acarreta et al.* [2004, equation (5)], the reflectance itself is fitted. The current DOAS equation requires a nonlinear fitting technique, but circumvents other issues, such as those associated with non-Gaussian noise after taking the logarithm of the background corrected signal. In addition to the use of a nonlinear fitting technique, a Ring spectrum is fitted to measurements as well. The reference Ring spectrum was obtained from a high-resolution solar spectrum using the methodology described by *Chance and Spurr* [1997].

[22] The reference spectrum of the O_2–O_2 absorption cross section measured by *Newnham and Ballard* [1998] was replaced with the spectrum measured by *Hermans et al.* [1999] (the spectra are available at http://www.oma.be/BIRA-IASB/Scientific/Topics/Lower/LaboBase/Laboratory.html). This change was made after comparing the O_2–O_2 absorption cross sections spectra measured by *Sneep et al.* [2006] with those by *Hermans et al.* [1999] and *Newnham and Ballard* [1998]. The first two spectra are in good agreement with each other. The choice was made to use the spectrum by *Hermans et al.* [1999] because of its dense wavelength coverage. No temperature dependence is included in the spectrum, because *Sneep et al.* [2006] have found that the changes in the O_2–O_2 absorption cross section over the temperature range present in the lower atmosphere are not significant.

[23] Another change concerns the surface albedo database used in the retrieval algorithm. The development version of the algorithm by *Acarreta et al.* [2004] used the GOME surface albedo database created by *Koelemeijer et al.* [2003]. The current operational retrieval scheme uses the spectral dependence of the GOME database, but scales the albedo itself to match the TOMS 340/380 nm database [*Herman and Celarier*, 1997], because of the much longer

Table 1. Parameters for the Synthetic Spectra Used in the Model Comparison[a]

	Label			
	1	2	3	4
Description	thin and low	thick and low	thin and high	thick and high
Cloud top	5 km	5 km	10 km	10 km
Cloud bottom	2 km	2 km	7 km	7 km
Total cloud optical thickness	9	42	9	42
Parameter	Measurement			
Oxygen A-band at 765 nm				
Spectral sampling	0.01 nm			
Surface albedo	0.0			
Oxygen CIA at 477 nm				
Spectral sampling	2 nm			
Surface albedo	0.05			
Raman scattering at 350 nm				
Surface albedo	0.05			

[a]The scenes we simulated using a scattering cloud (using a Henyey-Greenstein phase function with asymmetry parameter $g = 0.85$), and analyzed using the cloud models described in sections 3.1–3.3.

period over which those measurements were taken, thus minimizing cloud contamination.

3.3. OMI Cloud Pressure Retrieval Using the Filling in of Fraunhofer Lines by Rotational Raman Scattering at 350 nm

[24] Rotational-Raman scattering (RRS) causes filling in of solar Fraunhofer lines throughout the ultraviolet in the observed backscattered Earth radiance (normalized by the solar irradiance) [e.g., *Joiner et al.*, 1995]. This property was first used to retrieve an effective cloud pressure by *Joiner and Bhartia* [1995]. Spectral fitting methods that exploit the high-frequency spectral structure of RRS have been applied to hyperspectral instruments such as GOME and OMI [*Joiner et al.*, 2004; *Vasilkov et al.*, 2004; *Joiner and Vassilkov*, 2006]. The latter reference contains a description of a soft-calibration procedure that is used to remove scan position-dependent biases (i.e., striping) from the retrieved cloud pressures.

[25] The OMI RRS algorithm (officially named "OMCLDRR") is currently implemented with the same cloud model as the OMI O_2–O_2 cloud retrieval algorithm. There are two sets of products based on separate sets of assumptions applied to this model: The first set of products is included for historical reasons using a cloud albedo of 0.4 that produces an effective cloud fraction close to the MODIS geometrical cloud fraction. A second set is produced assuming a cloud albedo of 0.8 that gives cloud pressures closer to the physical cloud top at the lower cloud fractions. The latter set of products (called "CloudPressureforO3" and "CloudFractionforO3" in the OMCLDRR product files) is the one that will be used throughout this paper.

[26] These products are generated assuming a fixed surface albedo of 0.15 that was chosen to be consistent with the OMI total ozone retrieval based on the Total Ozone Mapping Spectrometer (TOMS) version 8 algorithm. This value is known to be higher than the actual surface albedo under most conditions but was designed to account for aerosol and small amounts of low-level cloud in the OMI TOMS-V8.

3.4. Comparison of PARASOL, OMCLDO2, OMCLDRR, and FRESCO Cloud Pressures Using Simulated Spectra

[27] To give a foundation to our expectations, four different cloud scenes were simulated for each of the cloud products. Although FRESCO [*Koelemeijer et al.*, 2001] is not part of the current comparison of observations, it is included here because both OMI cloud products were compared to it during the development phase using GOME measurements [*Acarreta et al.*, 2004; *Vasilkov et al.*, 2004]. All three algorithms (FRESCO, OMCLDO2 and OMCLDRR) have undergone significant upgrades since those articles were published, and a new investigation is warranted.

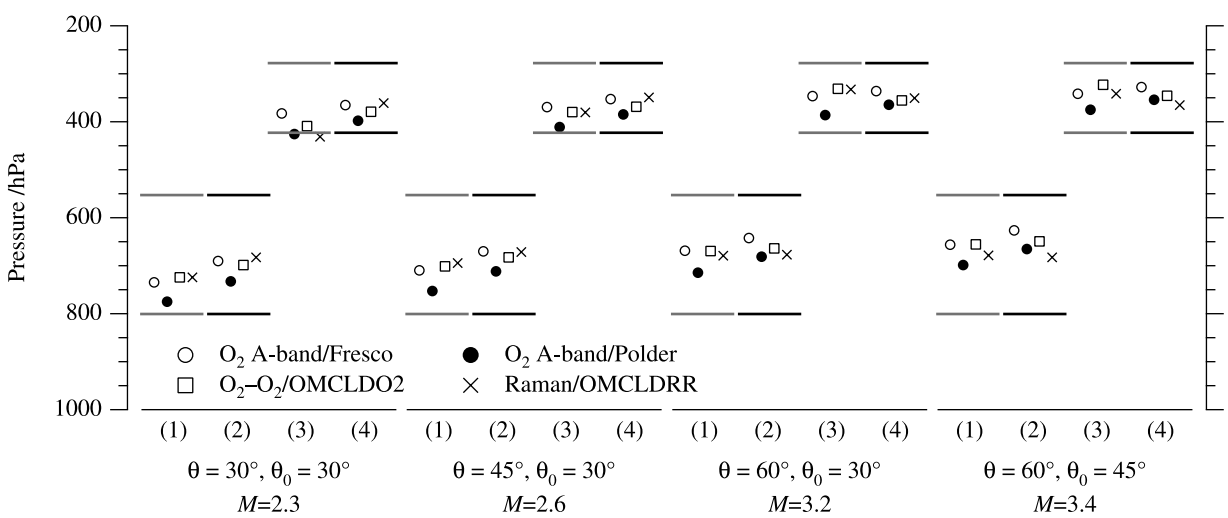

Figure 3. Cloud pressures retrieved from synthetic spectra for some selected solar and viewing angles, with the geometric air mass factor M indicated as well. The azimuth difference is 90° for all selected scenes. The numbers on the horizontal axes refer to the descriptions in Table 1.

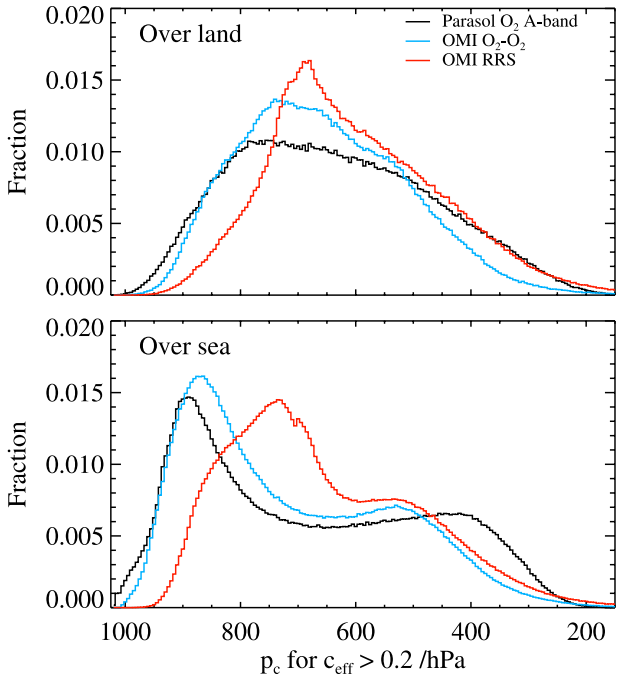

Figure 4. The distributions of cloud pressures from the OMI O_2–O_2, the OMI rotational Raman scattering, and the PARASOL O_2 A-band products, for scenes over (top) land and (bottom) sea.

[28] The absorption cross section of O_2–O_2 scales with the squared number density of oxygen. Some biases may be expected compared to FRESCO or the PARASOL oxygen cloud pressures, which use an absorption of single oxygen molecules. However, it must be understood that a significant portion of the signal in the O_2 A-band originates from the wings of the absorptions lines, since the line centers are mostly saturated. These wings also show a cross section that in first-order scales with the pressure squared, and therefore the differences between retrievals using O_2–O_2 at 477 nm and those using the O_2 A-band at 765 nm are smaller than might be expected initially.

[29] The cloud scenes used in this study are described in Table 1. The retrievals for PARASOL and FRESCO that are shown here are based on the same simulated spectra. For FRESCO the spectra are convolved with the GOME 2 slit function, followed by an analysis using the operational code. The same spectra were convolved with the instrument response function of PARASOL, and analyzed by the operational PARASOL code. To simplify the analysis, the calculations for PARASOL were done over a black surface, which removes the need for the surface correction. The O_2–O_2 band was simulated at a much lower spectral resolution; the shape of the absorption feature does not require the highest resolution. These synthetic spectra were generated using the DAK radiative transfer model. The RRS filling in was computed using the Linearized Discrete-Ordinate Radiative Transfer (LIDORT)-RRS model [*Spurr et al.*, 2008] and fed to an OMCLDRR cloud pressure retrieval simulator as described by *Vasilkov et al.* [2008].

[30] Results are shown for several viewing and solar geometries relevant for OMI and PARASOL in Figure 3. These results show that for all four retrieval techniques the retrieved cloud pressure is well below the cloud top. That a pressure well below the cloud top is found when the retrieval model uses a Lambertian cloud has been shown before [*Saiedy et al.*, 1967; *Koelemeijer et al.*, 2001; *Vanbauce et al.*, 1998, 2003; *Wang et al.*, 2006b; *Vasilkov et al.*, 2008], and is illustrated further in Figure 1. A decrease in the retrieved cloud pressure with increasing geometric air mass factor M can be seen, and for optically thick clouds a pressure level closer to the cloud top is found than for thinner clouds, in most cases.

[31] The difference between FRESCO and PARASOL in these simulations is up to 40 hPa, with FRESCO finding lower cloud pressures. Although both techniques are based on the O_2 A-band, the treatment of the spectrum is very different. The PARASOL retrieval technique has been described in section 3.1. Because of the spectral resolution available on GOME, SCIAMACHY, and GOME-2 for which FRESCO was developed, it is possible to fit some weak and strong parts in the O_2 A-band separately, rather than the whole band at once. This can lead to differences in the retrieved cloud pressure, even if the underlying spectra are the same. The cloud pressures found by FRESCO and OMCLDO2 are very close, to within 20 hPa, with no systematic bias. In these simulations OMCLDRR and OMCLDO2 are fairly close, although OMCLDRR seems to be more sensitive to the cloud optical thickness and air mass factor M. It seems that OMCLDRR finds pressures closer to the cloud top for

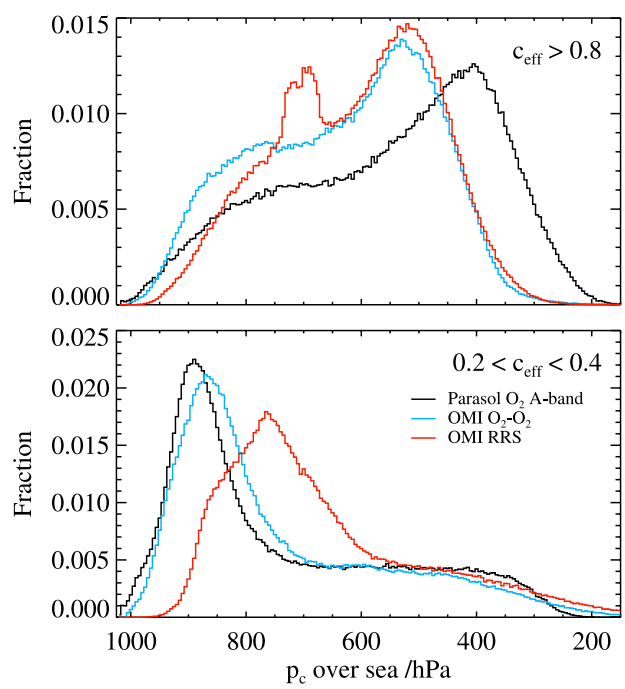

Figure 5. The distribution of cloud pressures from the OMI O_2–O_2, the OMI rotational Raman scattering, and the PARASOL O_2 A-band products, over sea for (top) scenes with a large effective cloud fraction and (bottom) scenes with a small effective cloud fraction.

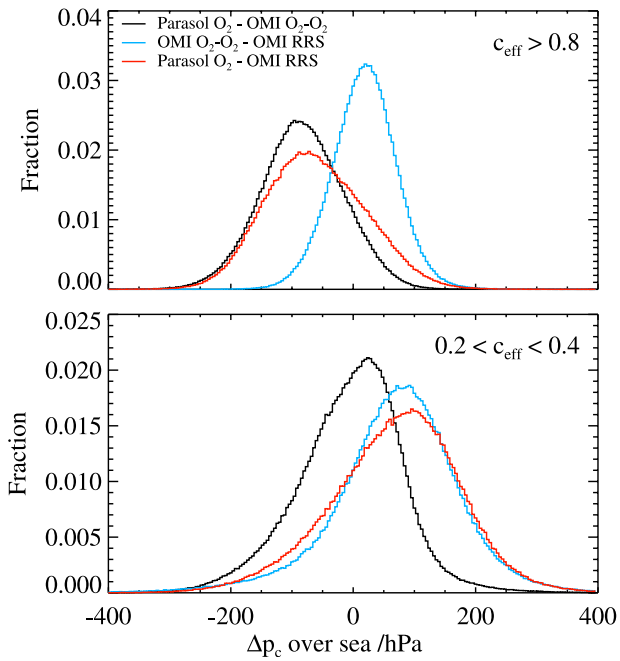

Figure 6. The distribution of differences in the cloud pressure between the O_2–O_2 cloud pressure and the rotational Raman scattering, both from OMI and the oxygen cloud pressure from PARASOL for colocated scenes over sea, for (top) scenes with a large effective cloud fraction and (bottom) scenes with a small effective cloud fraction.

thicker clouds at low M, and moves toward the bottom of the cloud for high M.

4. Data Selection

[32] The pixels on which PARASOL reports the cloud pressure are 18 × 18 km^2, comparable to the OMI nadir pixel size of 13 × 24 km^2. For this reason a one-to-one mapping between the two data sets was chosen, with a single PARASOL scene compared to a single OMI scene. For this article a special data set was prepared from the PARASOL data, where each orbit is stored in a separate file, rather than the standard single day in a file. This was done to avoid overlap of successive orbits at higher latitudes.

[33] This colocation procedure does not correct for partial geographical overlap for the pixels. A worst case scenario would have only 1/4 overlap between a PARASOL and an OMI pixel. To test the influence of the potential mismatch of the pixels, the comparisons were run on a single day of data, where the matches were deliberately offset by one pixel. The results from this comparison show that the RMS differences increased somewhat (from 74 to 89 hPa), but overall the results did not differ significantly from the main results presented here, indicating that an exact match on this spatial resolution is not critical.

[34] For this comparison a total of 383 orbits were used (OMI orbit numbers 9986 to 10 422, PARASOL repeat cycle 34, orbit 219 to cycle 36, orbit 189), covering most of June 2006. The software versions of the retrieval algorithms used to prepare the data are 1.0.1.1 for OMCLDO2, 1.2.0 for OMCLDRR, both operating on data from collection 2. The software release of PARASOL is 13.13. The measurements were filtered to exclude pixels over a bright surface by excluding snow or ice covered surfaces, on the basis of the NISE database [*Nolin et al.*, 2005] (updated daily). For these scenes it is known that the contrast between cloud cover and the surface is too low to properly distinguish clouds from the background, leading to an incorrect effective cloud fraction [*King et al.*, 1992], and therefore an ill-determined cloud pressure. Furthermore, the data were filtered to exclude pixels with a PARASOL cloud cover less than 95% as determined using the subpixels and the other channels of PARASOL [*Buriez et al.*, 1997]. Pixels where the rotational Raman effective cloud fraction is less than 0.2 were removed, because the rotational Raman algorithm switches to a different cloud model in those cases. After this filtering procedure, we are left with about 5.1 million colocated points.

5. Results and Discussion

[35] Histograms showing the global distribution of cloud pressures from the three retrieval methods are shown in Figure 4 separately for scenes over land and sea. Over sea a bimodal pressure distribution is found, while over land only a single mode is observed. Although the overall shape of the distribution of cloud pressures is very similar, some differences can be seen. To investigate where these differences occur, separate histograms are made for small ($0.2 \leq c_{\mathrm{eff}} < 0.4$) and large ($c_{\mathrm{eff}} > 0.8$) effective cloud fractions (from the OMI O_2–O_2 algorithm), shown in Figure 5. The distributions of the differences between the three cloud pressures are shown in Figure 6.

[36] Scatterplots of all combinations of the three parameters are shown in Figure 7, again separated for land and sea. The correlation coefficient ρ and the slope from a straight line fit including estimated errors in both data sets, following *Press et al.* [2003, section 15.3], are listed in each of the plots.

[37] Figure 8 shows the correlation coefficients, the median difference, and the 66% quantile width between all three data sets over land and over sea as a function of the effective cloud fraction. An increase in correlation with increasing c_{eff} is seen for land and sea. The results are summarized in Table 2.

[38] The three cloud pressure products are in good agreement, with average and RMS differences that are within the stated accuracy of those products. The PARASOL oxygen pressure accuracy is indicated by the observed standard deviation in the sequence of 16 consecutive measurements, which is typically in the order of 25 hPa. The OMI science requirements are 100 hPa [*Levelt et al.*, 2006a], and we consider the results presented here to be supportive in the claim that these requirements are met. Other comparisons and model studies [*Saiedy et al.*, 1967; *Koelemeijer et al.*, 2001; *Vanbauce et al.*, 1998, 2003; *Wang et al.*, 2006b; *Vasilkov et al.*, 2008, section 3.4] have shown that the cloud pressures derived from these techniques are mostly well inside the clouds. This is in strong contrast to thermal infrared observations, where the cloud top pressure is retrieved.

[39] Not only are the average differences and the spread in the differences within the cited requirements, the corre-

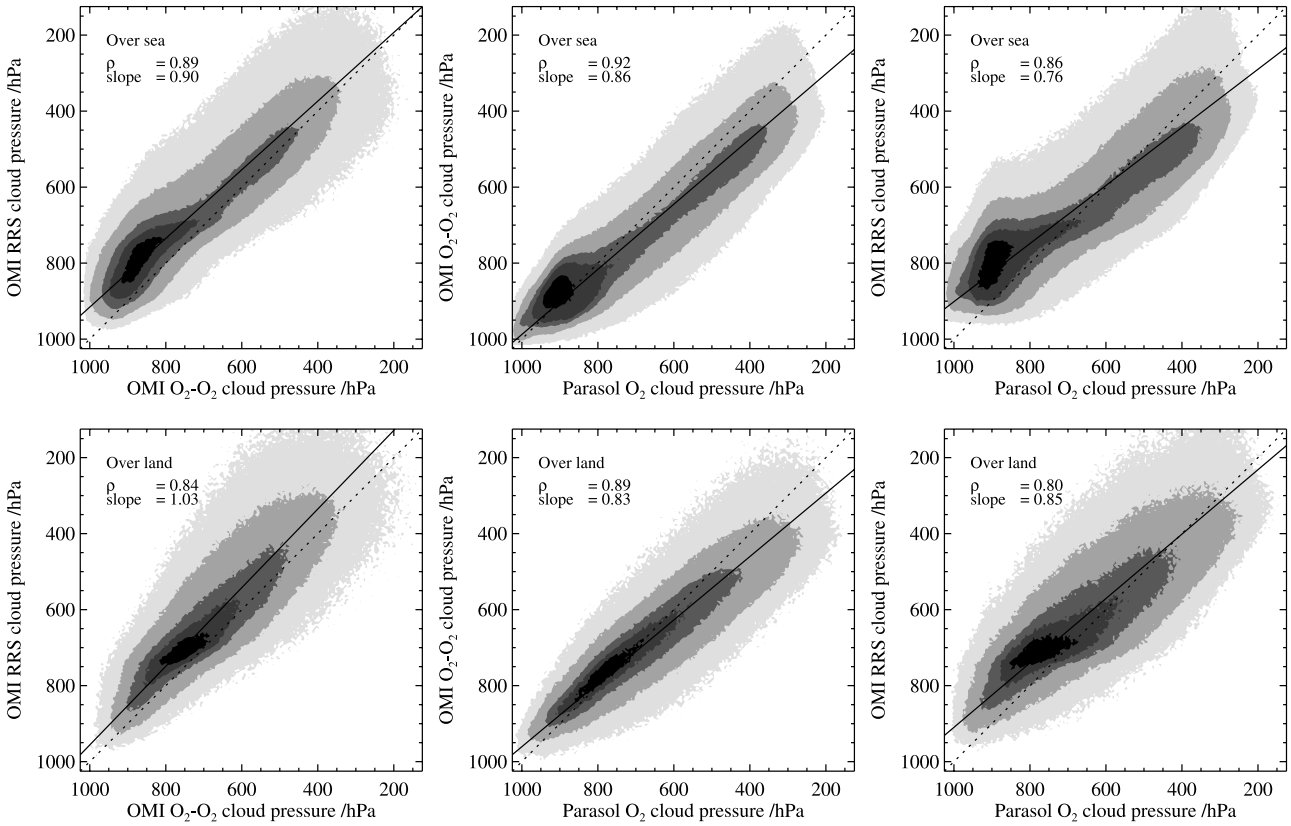

Figure 7. Probability distribution of the cloud pressure determined from OMI and PARASOL. The contours represent the densest area in the scatterplot, with the contours containing 10%, 30%, 60%, 90%, and 99% of all points, going to progressively lighter colors, for each of the three combinations of two algorithms. The data are shown separately for land and sea surfaces. The dotted line in each of the plots is the $x = y$ relation, and the solid line is the result of an orthogonal regression analysis, the slope of which is printed in each plot.

lation coefficients between the data sets, as listed in Table 2, are high and the slope observed in the scatterplots as shown in Figure 7, is reasonably close to 1, especially considering the time difference between the observations, giving confidence in all algorithms involved. Despite the similarities, there are details that stand out, and they will be discussed below.

[40] For low effective cloud fractions the two OMI cloud pressures can differ significantly, because of different assumptions about the surface albedo. The OMI O_2–O_2 algorithm uses a monthly surface albedo climatology derived from observations gridded to $1^\circ \times 1.25^\circ$, while the rotational Raman scattering algorithm uses a fixed value for the surface albedo of 0.15 which comes from the TOMS heritage. In a future version both will switch to a surface albedo climatology derived from OMI measurements at a higher spatial resolution. This will affect the cloud fraction most directly, but a change in effective cloud fraction will change the cloud pressure because the same strength of the spectral feature needs to be explained.

[41] From the distributions shown in Figure 4 and the scatterplots shown in Figure 7, in particular those over sea, one could conclude that the OMI O_2–O_2 cloud pressure retrieval shows a bias at low cloud pressures compared to the O_2 A-band retrieval from PARASOL. One might expect that this is caused by the pressure dependence of the absorption strength of the collision induced absorption ($\sigma_{O_2-O_2} \propto p^2$). On the other hand, rotational Raman scattering does not have a similar pressure dependence, and yet the retrieval based on RRS shows a similar behavior at low pressures over sea compared to the OMI O_2–O_2 cloud pressures. Model studies not presented here indicate that the influence of the quadratic pressure dependence of the O_2–O_2 cross section is limited to at most 40 hPa when compared to an absorber with a purely linear pressure dependence, which cannot explain the median difference between PARASOL and OMCLDO2 of ~80 hPa seen in Figure 7 for low-pressure clouds. Because the differences are most clearly seen over sea, we limited the next few steps to that subset.

[42] Further inspection of Figures 4 and 7, especially for scenes over sea, shows that for clouds at low pressures the PARASOL O_2 A-band algorithm retrieves smaller pressures than the OMI O_2–O_2 and RRS algorithms, with a difference of approximately 100 hPa for PARASOL pressures near 400 hPa. The distributions shown in Figure 5 indicate that the high clouds where the differences occur are also clouds with a high effective clouds fraction. The tails of the distributions at low pressure show very similar behavior for scenes with a small effective cloud fraction, but clearly

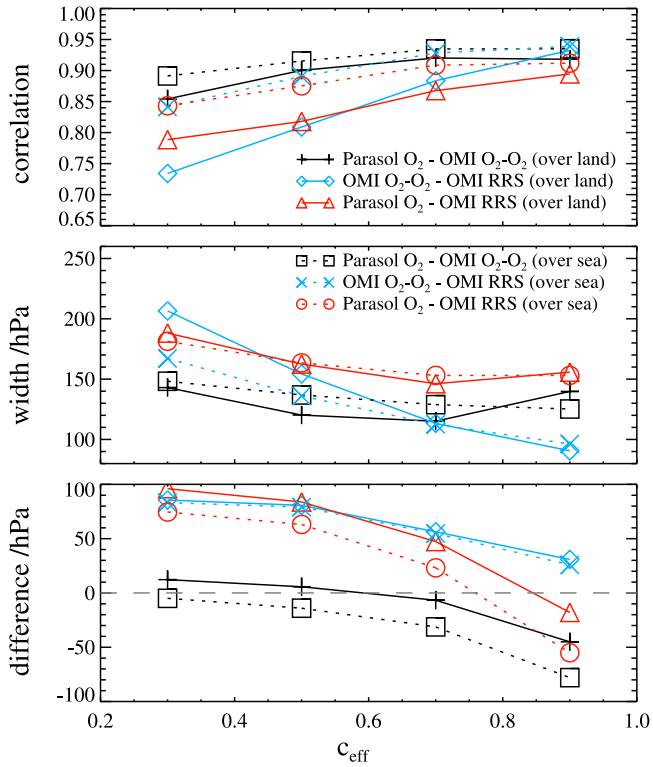

Figure 8. Correlation, 66% central quantile width, and median difference between all three combinations of cloud pressure products, over both land (solid lines) and sea (dashed lines), plotted as a function of the effective cloud fraction. The measurements were grouped by c_{eff}, from 0.2 to 0.4, from 0.4 to 0.6, from 0.6 to 0.8, and 0.8 and larger.

differ for scenes with a high effective cloud fraction; for small c_{eff} the differences occur at high pressure. The distribution of differences for the same data sets is shown in Figure 6. For high effective cloud fractions one can see that both OMI cloud pressures are in close agreement, with a close to normal distribution of the differences. The differences of PARASOL with either OMI cloud pressure for high effective cloud fraction show an offset of −100 hPa. For scenes with small c_{eff}, the OMI O_2–O_2 cloud pressure seems to agree best with PARASOL, while the OMI rotational Raman cloud pressure seems to be about 100 hPa lower than either.

[43] In the case of scenes with a large effective cloud fraction and low retrieved cloud pressure, we deal presumably with convective clouds with the cloud top located at low pressures, clouds that resemble case number (4) in the simulations shown in Figure 3. These simulations do not show the same bias that we observe here. What can be observed in Figure 3 is a decrease in the retrieved cloud pressure with increasing air mass factor M. Because of the multidirectional radiances measured by PARASOL, the geometric air mass is somewhat higher for PARASOL than for OMI. However, the differences in M are not large enough to explain the observed difference in the cloud pressure, and a detailed analysis looking into the variation of the cloud pressure observed from different angles does not show large variations either. In the work by *Fougnie et al.* [2007] the reflectance at which saturation occurs for each of the PARASOL bands is listed. For the broadband channel centered at 765 nm this happens at a reflectance of 0.96, while the narrow band saturates at a reflectance of 1.04. This means that the broadband channel will reach the regime where the CCD shows a nonlinear response much earlier than the narrowband channel, especially since the narrowband channel is mostly shielded by the O_2 A-band. A nonlinear response of the CCD can lead to an overestimation of the actual signal strength by up to 2–3% for strong signals [*Dobber et al.*, 2006; *Fougnie et al.*, 2007]. If a nonlinearity error of 2% is introduced in the simulations, the retrieved cloud pressures for PARASOL are reduced by 25 to 50 hPa for cases (2) and (4) shown in Figure 3. In light of the careful calibration of PARASOL as described by *Fougnie et al.* [2007], it seems unreasonable to completely attribute the observed differences between OMI and PARASOL in the cloud pressures for scenes with a high effective cloud fraction and at low cloud pressure to a nonlinear response of the detectors. However, we cannot exclude this possibility.

[44] The more frequent occurrence of clouds between 700 and 750 hPa in OMCLDRR, seen most clearly in the distribution for high effective cloud fractions shown in Figure 5 is unexplained. The presence of sun glint is expected to have opposing effects on both OMI products, causing a shift toward low pressures for RRS and a shift toward high pressures for O_2–O_2, but this cannot be present is scenes with high effective cloud fractions mentioned above. The effect of sun glint on the present analysis was investigated, and the correlation between the two OMI cloud pressures improved slightly for low cloud fractions when cases with possible sun glint are removed. No significant changes in the global statistical results were observed. Early results using the new collection 3 reprocessed level 1B radiances and irradiances show a more frequent occurrence of high-pressure clouds at low effective cloud fractions, bringing the distribution of OMCLDRR seen in Figure 5 closer to the other products.

[45] As an illustration of the observations by different A-train sensors we present results of the cloud pressure of Hurricane Ileana on 23 August 2006. This hurricane

Table 2. Some Statistical Parameters Describing the Differences of the Colocated Cloud Pressure Retrievals[a]

	PARASOL O_2 A	OMI O_2–O_2	OMI RRS
PARASOL O_2 A		$\overline{\Delta p_c}$ = 45 hPa $\sigma(\Delta p_c)$ = 74 hPa ρ = 0.93 slope = 1.19	$\overline{\Delta p_c}$ = 2 hPa $\sigma(\Delta p_c)$ = 93 hPa ρ = 0.88 slope = 1.32
OMI O_2–O_2	$\overline{\Delta p_c}$ = −45 hPa $\sigma(\Delta p_c)$ = 74 hPa ρ = 0.93 slope = 0.84		$\overline{\Delta p_c}$ = −44 hPa $\sigma(\Delta p_c)$ = 65 hPa ρ = 0.92 slope = 1.09
OMI RRS	$\overline{\Delta p_c}$ = −2 hPa $\sigma(\Delta p_c)$ = 93 hPa ρ = 0.88 slope = 0.76	$\overline{\Delta p_c}$ = 44 hPa $\sigma(\Delta p_c)$ = 65 hPa ρ = 0.92 slope = 0.92	
$\overline{p_c}$	642 hPa	687 hPa	644 hPa

[a]The difference is the product listed at the top minus the product listed at the left, and the slope is for the product listed at the top projected on the horizontal axis. This is for pixels over land and sea combined, filtered to include only pixels with $c_{\mathrm{eff}} > 0.5$.

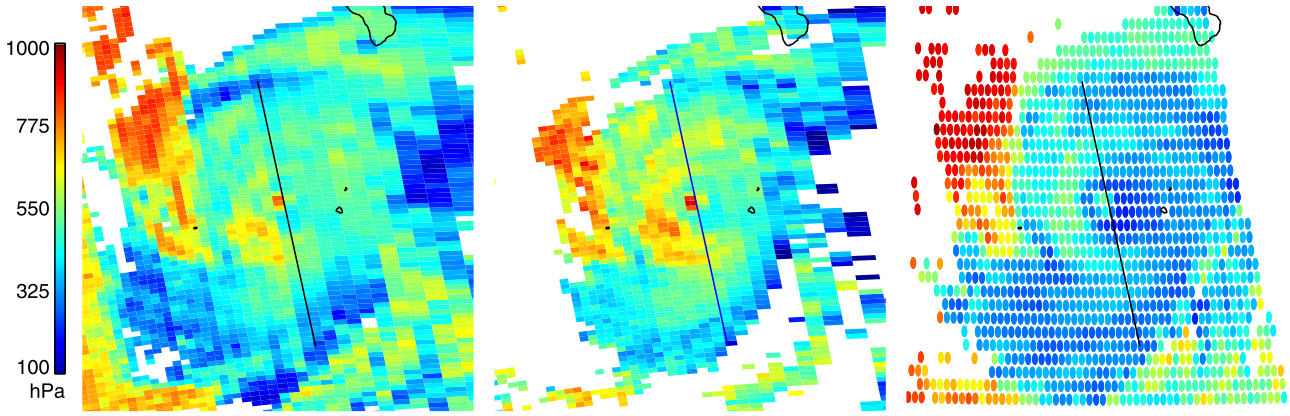

Figure 9. Cloud pressures in the hurricane Ileana, off the coast of Mexico, on 23 August 2006. (left) OMCLDO2, (middle) OMCLDRR, and (right) PARASOL cloud O_2 pressure. The solid line shows the path of CloudSat over the same hurricane; the CloudSat profiles are shown in Figure 1.

occurred west of the coast of Mexico. In Figure 9 the cloud pressure of the hurricane is shown from OMCLDO2, OMCLDRR, and PARASOL. The spiral structure of the hurricane is present in the cloud pressure of both products; the eye of the hurricane is also visible. CloudSat (15 min earlier than Aura) went right over the center of the hurricane making a vertical slice through it. This vertical cross section image is shown in Figure 1; the CloudSat radar reflectivity is shown in the color coding. One clearly sees that both OMI cloud pressures and the PARASOL oxygen cloud pressure are well inside the cloud system, whereas the MODIS cloud pressure, retrieved from IR channels, is at the top of the cloud system. The differences observed in Figures 5 and 7 between OMI and PARASOL for scenes with a high effective cloud fraction and a low retrieved cloud pressure can be observed in these profiles as well. Inside the eye of the hurricane the OMI and PARASOL cloud pressures are closer to the surface, whereas the MODIS cloud pressure, probably determined by cirrus, is still close to the top of the cloud system. Figure 1 empirically demonstrates what was expected from the simulations presented in section 3.4, namely that the cloud pressure retrieval methods using UV-visible back-scattered radiation and a Lambertian cloud model, like OMI O_2–O_2, OMI RRS and PARASOL O_2, yield a pressure level inside the cloud. Methods using emitted thermal IR radiation, like MODIS, yield a cloud pressure level at the top, as expected.

[46] Figure 8 and Table 2 serve as a summary of our observations. For high effective cloud fractions we see a higher correlation between all three cloud pressures, both over land and over sea. This is as expected, as more clouds will give a better determination of the cloud pressure, and far less influence of the surface albedo. In line with the above observations, the width of the distribution of differences also reduces as the effective cloud fraction increases. The median differences reported in Figure 8 show systematic differences between PARASOL and both OMI pressures whatever the effective cloud fraction. Indeed while the differences between the two OMI cloud pressures obtained over land and over sea are almost identical, the difference between PARASOL and OMI pressures observed over land are 10 to 40 hPa higher than those observed over sea. As the OMI pressure retrievals are spectrally less sensitive to the surface albedo than the PARASOL ones such differences may reveal that the PARASOL surface-corrected pressures are overestimated from 10 to 40 hPa. Note that without this surface correction the PARASOL apparent pressure can be so high that the retrieved level is far (typically 100 hPa) below the cloud base [*Vanbauce et al.*, 2003]. Only a complete validation with help of active instruments as Caliop and CloudSat will provide us enough information on cloud boundaries to accurately know where in the cloud layer are the retrieved pressures. A qualitative start of such a validation is shown in Figure 1.

[47] We have performed a limited model study to help explain the observed differences between the three cloud products. Our model calculations were not able to explain the differences between PARASOL and the OMI pressures that are present particularly for very bright clouds. More research, including radiative transfer calculations for multiple cloud decks and clouds of varying geometrical and optical thickness, are needed to fully understand the differences between the algorithms. Both OMI algorithms will be updated in the near future. The updates will include new surface albedo data sets and will use the new calibration that is included in the collection 3 L1B data set.

[48] **Acknowledgments.** We thank the anonymous reviewers for their critical comments and suggestions for improving earlier versions of the manuscript. The OMI and PARASOL science teams are gratefully acknowledged. The work at KNMI was funded by the Space Research Organisation of the Netherlands (SRON) under grant EO-072. The work at Laboratoire d'Optique Atmosphérique (LOA) was supported by the Centre National d'Etudes Spatiales (CNES) and Région Nord-Pas de Calais. This material is based in part upon work supported by NASA under agreement NNG06HX18C issued through the Science Mission Directorate for the EOS Aura Science Team. We thank the NASA CloudSat project for making available the CloudSat data used in this paper. The authors would like to thank Frédéric Parol for helpful discussions, François Thieuleux for all PARASOL data processing, and Quintus Kleipool for dicussions on the nonlinear behavior of CCDs.

References

Acarreta, J. R., J. F. de Haan, and P. Stammes (2004), Cloud pressure retrieval using the O_2-O_2 absorption band at 477 nm, *J. Geophys. Res.*, *109*, D05204, doi:10.1029/2003JD003915.

Ahmad, Z., P. K. Bhartia, and N. Krotkov (2004), Spectral properties of backscattered UV radiation in cloudy atmospheres, *J. Geophys. Res.*, *109*, D01201, doi:10.1029/2003JD003395.

Buriez, J.-C., C. Vanbauce, F. Parol, P. Goloub, M. Herman, B. Bonnel, Y. Fouquart, P. Couvert, and G. Sèze (1997), Cloud detection and derivation of cloud properties from POLDER, *Int. J. Remote Sens.*, *18*, 2785–2813.

Buriez, J.-C., F. Parol, C. Cornet, and M. Doutriaux-Boucher (2005), An improved derivation of the top-of-atmosphere albedo from POLDER/ADEOS-2: Narrowband albedos, *J. Geophys. Res.*, *110*, D05202, doi:10.1029/2004JD005243.

Chance, K. V., and R. J. D. Spurr (1997), Ring effect studies: Rayleigh scattering, including molecular parameters for rotational Raman scattering, and the Fraunhofer spectrum, *Appl. Opt.*, *36*, 5224–5230.

Clothiaux, E. E., T. P. Ackerman, G. G. Mace, K. P. Moran, R. T. Marchand, M. A. Miller, and B. E. Martner (2000), Objective determination of cloud heights and radar reflectivities using a combination of active remote sensors at the ARM CART sites, *J. Appl. Meteorol.*, *39*, 645–665.

de Haan, J. F., P. B. Bosma, and J. W. Hovenier (1987), The adding method for multiple scattering calculations of polarized light, *Atron. Astrophys.*, *183*, 371–393.

Deschamps, P., F. Breon, M. Leroy, A. Podaire, A. Bricaud, J.-C. Buriez, and G. Sèze (1994), The POLDER mission: Instrument characteristics ans scientific objectives, *IEEE Trans. Geosci. Remote Sens.*, *32*, 598–615.

Dobber, M. R., et al. (2006), Ozone monitoring instrument calibration, *IEEE Trans. Geosci. Remote Sens.*, *44*, 1209–1238.

Fougnie, B., G. Bracco, B. Lafrance, C. Ruffel, O. Hagolle, and C. Tinel (2007), PARASOL in-flight calibration and performance, *Appl. Opt.*, *46*, 5435–5451.

Greenblatt, G. D., J. J. Orlando, J. B. Burkholder, and A. R. Ravishankara (1990), Absorption measurements of oxygen between 330 and 1140 nm, *J. Geophys. Res.*, *95*, 18,577–18,582.

Herman, J. R., and E. A. Celarier (1997), Earth surface reflectivity climatology at 340–380 nm from TOMS data, *J. Geophys. Res.*, *102*, 28,003–28,012.

Hermans, C., A. Vandaele, M. Carleer, S. Fally, R. Colin, A. Jenouvrier, B. Coquart and M.-F. Mérienne (1999), Absorption cross-sections of atmospheric constituents: NO_2, O_2, and H_2O, *Environ. Sci. Pollut. Res.*, *6*, 151–158.

Joiner, J., and P. K. Bhartia (1995), The determination of cloud pressures from rotational Raman scattering in satellite backscatter ultraviolet measurements, *J. Geophys. Res.*, *100*, 23,019–23,026.

Joiner, J., and A. P. Vassilkov (2006), First results from the OMI rotational Raman scattering cloud pressure algorithm, *IEEE Trans. Geosci. Remote Sens.*, *44*, 1272–1282.

Joiner, J., P. K. Bhartia, R. P. Cebula, E. Hilsenrath, R. D. McPeters, and H. Park (1995), Rotational-Raman scattering (Ring effect) in satellite backscatter ultraviolet measurements, *Appl. Opt.*, *34*, 4513–4525.

Joiner, J., A. P. Vasilkov, D. E. Flittner, J. F. Gleason, and P. K. Bhartia (2004), Retrieval of cloud pressure and oceanic chlorophyll content using Raman scattering in GOME ultraviolet spectra, *J. Geophys. Res.*, *109*, D01109, doi:10.1029/2003JD003698.

King, M. D., Y. J. Kaufman, W. P. Menzel, and D. Tanré (1992), Remote sensing of cloud, aerosol, and water vapor properties from the moderate resolution imaging spectrometer (MODIS), *IEEE Trans. Geosci. Remote Sens.*, *30*, 1–27.

Koelemeijer, R. B. A., and P. Stammes (1999), Effects of clouds on ozone column retrieval from GOME UV measurements, *J. Geophys. Res.*, *104*, 8281–8294.

Koelemeijer, R. B. A., P. Stammes, J. W. Hovenier, and J. F. de Haan (2001), A fast method for retrieval of cloud parameters using oxygen A-band measurements from GOME, *J. Geophys. Res.*, *106*, 3475–3490.

Koelemeijer, R. B. A., J. F. de Haan, and P. Stammes (2003), A database of spectral surface reflectivity in the range 335–772 nm derived from 5.5 years of GOME observations, *J. Geophys. Res.*, *108*(D2), 4070, doi:10.1029/2002JD002429.

Levelt, P. F., E. Hilsenrath, G. W. Lepppelmeier, G. H. J. van den Oord, P. K. Bhartia, J. Taminnen, J. F. de Haan, and J. P. Veefkind (2006a), Science objectives of the Ozone Monitoring Instrument, *IEEE Trans. Geosci. Remote Sens.*, *44*, 1199–1208.

Levelt, P. F., G. H. J. van den Oord, M. R. Dobber, A. Malkki, H. Visser, J. de Vries, P. Stammes, J. Lundell, and H. Saari (2006b), The Ozone Monitoring Instrument, *IEEE Trans. Geosci. Remote Sens.*, *44*, 1093–1101.

Liu, X., M. J. Newchurch, R. Loughman, and P. K. Bhartia (2004), Errors resulting from assuming opaque Lambertian clouds in TOMS ozone retrieval, *J. Quant. Spectrosc. Radiat. Transfer*, *85*, 337–365.

Newnham, D. A., and J. Ballard (1998), Visible absorption cross sections and integrated absorption intensities of molecular oxygen (O_2 and O_4), *J. Geophys. Res.*, *103*(D22), 28,801–28,815.

Nolin, A., R. Armstrong, and J. Maslanik (2005), Near real-time SSM/I EASE-grid daily global ice concentration and snow extent, http://nsidc.org/data/nise1.html, Natl. Snow and Ice Data Cent., Boulder, Colo.

Platt, U. (1994), Differential optical absorption spectroscopy (DOAS), in *Air Monitoring by Spectroscopic Techniques*, *Chem. Anal. Ser.*, vol. 127, edited by M.W. Sigrist, chap. 2, pp. 27–84, John Wiley, Hoboken, N.J.

Press, W. H., S. A. Teukolsky, W. T. Vetterling, and B. P. Flannery (2003), Numerical Recipes in Fortran 77: The Art of Scientific Computing, 2nd ed., Cambridge Univ. Press, New York.

Rothman, L. S., et al. (2005), The HITRAN 2004 molecular spectroscopic database, *J. Quant. Spectrosc. Radiat. Transfer*, *96*, 139–204.

Saiedy, F., H. Jacobowitz, and D. Wark (1967), On cloud-top determination from Gemini-5, *J. Atmos. Sci.*, *24*, 63–69.

Scott, N. A. (1974), A direct method of computation of the transmission function of an inhomogeneous gaseous medium. I: Description of the method, *J. Quant. Spectrosc. Radiat. Transfer*, *14*, 691–704.

Sneep, M., D. Ityaksov, I. Aben, H. Linnartz, and W. Ubachs (2006), Temperature-dependent cross sections of O_2-O_2 collision-induced absorption resonances at 477 and 577 nm, *J. Quant. Spectrosc. Radiat. Transfer*, *98*, 405–424.

Spurr, R., J. F. de Haan, R. van Oss, and A. Vasilkov (2008), Discrete ordinate radiative transfer in a stratified medium with first order rotational Raman scattering, *J. Quant. Spectrosc. Radiat. Transfer*, *109*, 404–425, doi:10.1016/j.jqsrt.2007.08.011.

Stammes, P. (2001), Spectral radiance modeling in the UV-visible range, in IRS200: Current Problems in Atmospheric Radiation, edited by W. L. Smith and Y. M. Timofeyev, pp. 385–388, A. Deepak, Hampton, Va.

Stammes, P., M. Sneep, J. Joiner, A. P. Vasilkov, J. F. de Haan, J. P. Veefkind, G. Labow, P. F. Levelt, and P. K. Bhartia (2008), Effective cloud fractions from OMI: Theoretical framework and validatio, *J. Geophys. Res.*, doi:10.1029/2007JD008820, in press.

Vanbauce, C., J. Buriez, F. Parol, B. Bonnel, G. Sèze, and P. Couvert (1998), Apparent pressure derived from ADEOS-POLDER observations in the oxygen A-band over ocean, *Geophys. Res. Lett.*, *25*, 3159–3162.

Vanbauce, C., B. Cadet, and R. T. Marchand (2003), Comparison of POLDER apparent and corrected oxygen pressure to ARM/MMCR cloud boundary pressures, *Geophys. Res. Lett.*, *30*(5), 1212, doi:10.1029/2002GL016449.

Vasilkov, A. P., J. Joiner, K. Yang, and P. K. Bhartia (2004), Improving total column ozone retrievals by using cloud pressures derived from Raman scattering in the UV, *Geophys. Res. Lett.*, *31*, L20109, doi:10.1029/2004GL020603.

Vasilkov, A. P., J. Joiner, R. Spurr, P. K. Bhartia, P. F. Levelt, and G. Stephens (2008), Evaluation of the OMI cloud pressures derived from rotational Raman scattering by comparisons with other data and radiative transfer simulations, *J. Geophys. Res.*, doi:10.1029/2007JD008689, in press.

Wang, P., P. Stammes, and K. F. Boersma (2006a), Impact of the effective cloud fraction assumption on tropospheric NO_2 retrievals, in Proceedings of the First Conference on Atmospheric Science, Eur. Space Agency Spec. Publ., ESA SP-628, p4–38.

Wang, P., P. Stammes, and N. Fournier (2006b), Test and first validation of FRESCO+, *Proc. SPIE Int. Soc. Opt. Eng.*, *6362*, 13–20.

J. F. de Haan, P. F. Levelt, M. Sneep, P. Stammes, and P. Wang, Climate Research and Seismology Department, Royal Netherlands Meteorological Institute, P.O. Box 201, NL-3730 AE De Bilt, Netherlands. (maarten.sneep@knmi.nl; stammes@knmi.nl)

J. Joiner, NASA Goddard Space Flight Center, Greenbelt, MD 20771, USA. (joanna.joiner@nasa.gov)

C. Vanbauce, Laboratoire d'Optique Atmosphérique, Université des Sciences et Technologies de Lille, CNRS, F-59655 Villeneuve d'Ascq CEDEX, France. (claudine.vanbauce@loa.univ-lille1.fr)

A. P. Vasilkov, Science Systems and Applications, Inc., Lanham, MD 20706, USA.